

See discussions, stats, and author profiles for this publication at: <https://www.researchgate.net/publication/343812312>

Non-Negative Intensity for Planar Structures Under Stochastic Excitation

Article in *Journal of Sound and Vibration* · August 2020

DOI: 10.1016/j.jsv.2020.115652

CITATIONS

0

READS

71

5 authors, including:



Mahmoud Karimi

University of Technology Sydney

36 PUBLICATIONS 245 CITATIONS

[SEE PROFILE](#)



Laurent Maxit

Institut National des Sciences Appliquées de Lyon

113 PUBLICATIONS 807 CITATIONS

[SEE PROFILE](#)



Valentin Meyer

Naval Group Research

27 PUBLICATIONS 65 CITATIONS

[SEE PROFILE](#)



Steffen Marburg

Technische Universität München

265 PUBLICATIONS 3,241 CITATIONS

[SEE PROFILE](#)

Some of the authors of this publication are also working on these related projects:



Quantifying the performance of natural ventilation windcatchers [View project](#)



Laser Doppler Vibrometry from Vibrating Platforms [View project](#)

Non-Negative Intensity for Planar Structures Under Stochastic Excitation

M. Karimi^{1*}, L. Maxit², V. Meyer³, S. Marburg⁴, R. Kirby¹

¹ *Centre for Audio, Acoustics and Vibration, University of Technology Sydney, Sydney, Australia*

² *Univ Lyon, INSA-Lyon, Laboratoire Vibrations-Acoustique (LVA), 25 bis, av. Jean Capelle, F-69621, Villeurbanne Cedex, France*

³ *Naval Group Research, 199 avenue Pierre-Gilles de Gennes, 83190 Ollioules, France*

⁴ *Chair of Vibroacoustics of Vehicles and Machines, Department of Mechanical Engineering, Technische Universität München, München, Germany*

Abstract

Identification of regions on a vibrating structure which radiate energy to the far field is critical in many areas of engineering. Non-negative intensity is a means to visualize contributions of local surface regions to sound power from vibrating structures. Whilst the non-negative intensity has been used for structures under deterministic excitation due to structural forces or harmonic incident acoustic pressure excitation, it has not been considered for analyzing a structure under stochastic excitation. This work analytically formulates non-negative intensity in the wavenumber domain to investigate the surface areas on a vibrating planar structure that are contributing to the radiated sound power in the far field. The non-negative intensity is derived in terms of the cross spectrum density function of the stochastic field and the sensitivity functions of either the acoustic pressure or normal fluid particle velocity. The proposed formulation can be used for both infinite planar structure and finite plate in an infinite baffle. To demonstrate the technique, a simply supported baffled panel excited by a turbulent boundary layer as well as an acoustic diffuse field is considered and those regions contributing to the radiated sound power are identified. It is demonstrated that the non-negative intensity distribution is dependent on the stochastic excitation. It is also found that for a panel under stochastic excitation the more the non-negative intensity distribution is concentrated within the panel surface, the

*Corresponding author

Email address: Mahmoud.karimi@uts.edu.au

more efficient the panel radiates sound to the far field.

Keywords: Acoustic radiation, non-negative intensity, surface contribution, stochastic excitation, turbulent boundary layer, acoustic diffuse field

1. INTRODUCTION

Reconstruction techniques of sound sources such as near-field acoustic holography (NAH), inverse boundary element method (BEM) and the equivalent sources methods are widely used in industry [1]. In many engineering applications, it is important to identify the regions on a vibrating structure which radiate energy to the far field. This identification can help design engineers to gain a deeper understanding about the noise generation mechanism, and it also allows targeted mitigation strategies to be explored. For example, noise reduction can be achieved by modifying geometry and structural properties. Acoustic intensity can help with identifying hot spots on the structure. However, intensity is usually highly bipolar and has positive and negative values that correspond to energy sources and sinks on the surface of the radiating structure. Therefore, the near-field cancellation effects occur when integrating the positive and negative components of the normal acoustic intensity over the surface of the structure. Williams [2; 3] introduced the supersonic intensity (SSI) formulation in the wavenumber domain. The SSI was employed to locate the areas on the source surface which effectively contribute to the far-field pressure. The SSI eliminates the contribution to the pressure and the velocity on the source of the high wavenumber components (subsonic components), which are evanescent and do not contribute to the far field. The modified velocity and pressure obtained by considering only the wavenumber in the acoustic circle were termed supersonic velocity and supersonic pressure respectively.

The SSI was computed in the space domain using a two-dimensional convolution between the acoustic field and a spatial filter mask by Fernandez-Grande et al. [4]. The filter corresponds to the space domain representation of the acoustic circle. Hence, only the acoustic waves that propagate effectively to the far field were taken into account. The numerical technique was validated by an experimental study on planar radiators. Fernandez-Grande and Jacobsen [5] quantitatively examined the accuracy of the supersonic intensity. They quantified the error introduced by the finite measurement aperture. It was demonstrated that the error was substantial at low frequen-

33 cies. The study showed that using an extended aperture and/or an increased
34 cut-off frequency the error can be diminished. Valdivia et al. [6] employed
35 supersonic acoustic intensity to locate radiating regions on a vibrating struc-
36 ture of arbitrarily shaped geometries. They removed the evanescent waves
37 from the NAH measurement. A method based on a stable invertible repre-
38 sentation of the radiated power operator was proposed. The stable invertible
39 operator was derived using the equivalent source formulation and a complete
40 spectral basis. The proposed method was validated using experimental data
41 from a vibrating ship-hull structure.

42 Magalhães and Tenenbaum [7] extended the SSI technique to consider
43 arbitrarily shaped sources. Their work was based on the BEM and singu-
44 lar value decomposition. Marburg et al. [8] formulated the non-negative
45 intensity (NNI) using the BEM to identify the surface areas of a vibrating
46 structure that contribute to the radiated sound power. The acoustic ra-
47 diation modes were employed to compute the surface contributions of the
48 structure for all boundaries of the acoustic domain. Williams [9] proposed
49 two analytical formulae for the NNI based on the pressure and normal fluid
50 particle velocity for planar structures under deterministic excitation. It was
51 shown that both formulae yield almost identical results in prediction of the
52 regions of a structure that emit sound to the far field.

53 Junior and Tenenbaum [10] proposed an equivalent technique to the SSI
54 based on the BEM called useful intensity. The technique does not require the
55 construction of a hologram to evaluate the acoustic pressure from the known
56 normal velocity field on the vibrating surface. Both the analytical SSI and
57 the numerical useful intensity methods were used by Ferreira et al. [11] to
58 examine the sound radiated from rectangular baffled panels. Eight differ-
59 ent combinations of classical boundary conditions were considered. It was
60 shown that the results obtained using the useful intensity were not strictly
61 the same as those obtained using the SSI. The NNI based on the BEM was
62 also employed to identify the surface areas of a rigid sphere and a rigid cylin-
63 der that contributes to the scattered sound power [12]. The same technique
64 was applied to localize the surface areas of vibrating structure to radiated
65 sound power [13; 14]. The surface contribution from a panel to the radiated
66 sound power for different modes was numerically investigated [14]. The nu-
67 merical results were validated by NAH measurements. Similar distributions
68 of numerical and experimental NNI were observed at each mode. Liu et al.
69 [15] used the NNI based on the BEM to investigate the effect of inhomog-
70 eneous Rayleigh damping on the surface contributions to radiated sound

71 power. It was found that traveling waves propagate to the regions with
72 higher damping. Wilkes et al. [16] applied the NNI method to a fluid-loaded
73 steel spherical shell excited by a point/ring force. A hybrid finite element
74 and fast multipole boundary element method (FMBEM) was used to solve
75 the structural-acoustic problem. The boundary field was then used in the
76 FMBEM solver to compute the NNI.

77 Identification of source velocities on 3D structures in non-anechoic en-
78 vironments using the inverse patch transfer functions (IPTF) method was
79 first introduced by Aucejo et al. [17]. The direct patch transfer functions
80 method can be used to predict the structural velocity or the sound pressure
81 of a domain containing acoustic sources by calculating acoustic impedances
82 of uncoupled sub-domains. The IPTF method can identify the unknown
83 sources by measuring the coupling velocity at an arbitrarily defined surface
84 surrounding the source. Vigoureux et al. [18] investigated rigorous crite-
85 ria needed to obtain accurate results using IPTF to identify sources in a
86 non-anechoic or reverberant environment on an irregularly shaped structure.
87 Further, a procedure was proposed to compute intensity of the source and
88 wall pressure without any additional measurement. A frequency band was
89 detected for which the IPTF method was not providing accurate results.
90 This was attributed to the presence of evanescent waves. Valdivia [19; 20]
91 developed a method based on the spectral decomposition of the power op-
92 erator that yielded an NNI expression to efficiently compute the supersonic
93 components from acoustic pressure measurements for arbitrary geometries.
94 Using numerical models it was shown that the proposed NNI matched the
95 SSI.

96 Stochastic excitations such as turbulent boundary layer (TBL) and acous-
97 tic diffuse field (ADF) are widely encountered in transportation systems [21–
98 23]. For example, aircraft, satellite, marine vessels, high speed trains and
99 cars are subject to random and non-deterministic excitations throughout
100 their operations. While surface contribution techniques such as the SSI and
101 NNI have been developed for structures under deterministic excitation, they
102 have not been applied for analyzing a structure under stochastic excitation.
103 In this work, the NNI is analytically formulated for planar structures under
104 stochastic excitation in the wavenumber domain. The proposed formulation
105 is valid for both infinite planar structure and finite plate in an infinite baffle.
106 Two formulae are developed for the NNI which are in terms of the cross spec-
107 trum density function of the stochastic field and the sensitivity functions of
108 either the acoustic pressure or normal fluid particle velocity. The technique

109 is implemented to identify the regions of a vibrating simply supported baf-
 110 fled panel contributing to the radiated sound power. Both TBL and ADF
 111 excitations are considered to illustrate the proposed technique.

112 2. Radiated Acoustic Power

The radiated acoustic power of an infinite planar structure or a finite plate in an infinite baffle under stochastic excitation can be obtained by integrating the normal active intensity I_{act} , corresponding to the cross spectrum between the sound pressure and the normal fluid particle velocity denoted by S_{pv_f} , over the infinite boundary surface as follows [24; 25]

$$\Pi_{\text{rad}}(\omega) = \int_{\infty} I_{\text{act}} d\mathbf{x} = \int_{\infty} \text{Re} \{ S_{pv_f}(\mathbf{x}, \omega) \} d\mathbf{x}, \quad (1)$$

where $\mathbf{x} = (x, y)$, and ω is the angular frequency. The cross spectrum is given by the following analytical expression [25]

$$S_{pv_f}(\mathbf{x}, \omega) = \frac{1}{4\pi^2} \int_{\infty} H_p(\mathbf{x}, \mathbf{k}, \omega) H_v^*(\mathbf{x}, \mathbf{k}, \omega) \phi_{pp}(\mathbf{k}, \omega) d\mathbf{k}, \quad (2)$$

113 where * denotes the complex conjugate. $H_p(\mathbf{x}, \mathbf{k}, \omega)$, $H_v(\mathbf{x}, \mathbf{k}, \omega)$ are sensi-
 114 tivity functions for the radiated pressure and the normal fluid particle ve-
 115 locity on the surface of structure, respectively. The sensitivity functions in
 116 the spatial domain are related to the spectral sensitivity functions in the
 117 wavenumber domain $\tilde{\mathbf{k}}$, denoted by $\tilde{H}_p(\tilde{\mathbf{k}}, \mathbf{k}, \omega)$ and $\tilde{H}_v(\tilde{\mathbf{k}}, \mathbf{k}, \omega)$, by inverse
 118 Fourier transform as follows

$$H_p(\mathbf{x}, \mathbf{k}, \omega) = \frac{1}{4\pi^2} \int_{\infty} \tilde{H}_p(\tilde{\mathbf{k}}, \mathbf{k}, \omega) e^{i\tilde{\mathbf{k}}\mathbf{x}} d\tilde{\mathbf{k}}, \quad (3)$$

$$H_v^*(\mathbf{x}, \mathbf{k}, \omega) = \frac{1}{4\pi^2} \int_{\infty} \tilde{H}_v^*(\tilde{\mathbf{k}}, \mathbf{k}, \omega) e^{-i\tilde{\mathbf{k}}\mathbf{x}} d\tilde{\mathbf{k}}. \quad (4)$$

119 Using Eqs. (1)-(4), the radiated acoustic power of a planar structure under
 120 stochastic excitation can be written as follows [26]

$$\Pi^{\text{rad}}(\omega) = \text{Re} \left[\left(\frac{1}{4\pi^2} \right)^2 \int_{\infty} \int_{\infty} \tilde{H}_p(\tilde{\mathbf{k}}, \mathbf{k}, \omega) \tilde{H}_v^*(\tilde{\mathbf{k}}, \mathbf{k}, \omega) \phi_{pp}(\mathbf{k}, \omega) d\mathbf{k} d\tilde{\mathbf{k}} \right], \quad (5)$$

121 where $\phi_{pp}(\mathbf{k}, \omega)$ is the cross spectrum density (CSD) function of the stochastic
 122 force. The sensitivity function of the normal fluid particle velocity on the
 123 panel surface is related to the sensitivity function of the sound pressure in
 124 the wavenumber domain as follows [24]

$$\tilde{H}_p(\tilde{\mathbf{k}}, \mathbf{k}, \omega) = \frac{\rho_a \omega}{\tilde{k}_z(\tilde{\mathbf{k}})} \tilde{H}_v(\tilde{\mathbf{k}}, \mathbf{k}, \omega), \quad (6)$$

125 where

$$\tilde{k}_z(\tilde{\mathbf{k}}) = \left\{ \begin{array}{ll} \sqrt{k_a^2 - \tilde{k}_x^2 - \tilde{k}_y^2}, & k_a^2 \geq \tilde{k}_x^2 + \tilde{k}_y^2 \\ i\sqrt{\tilde{k}_x^2 + \tilde{k}_y^2 - k_a^2}, & \text{otherwise} \end{array} \right\}, \quad (7)$$

126 and k_a is the acoustic wavenumber, ρ_a is the fluid density, and $\tilde{\mathbf{k}} = (\tilde{k}_x, \tilde{k}_y)$.
 127 Substituting Eq. (6) in Eq. (5), the radiated acoustic power can be written
 128 either in terms of sound pressure or normal fluid particle velocity sensitivity
 129 functions as follows

$$\Pi_p^{\text{rad}}(\omega) = \text{Re} \left[\frac{1}{16\pi^4 \rho_a \omega} \int_{-\infty}^{\infty} \int_{-\infty}^{\infty} \tilde{k}_z^*(\tilde{\mathbf{k}}) \left| \tilde{H}_p(\tilde{\mathbf{k}}, \mathbf{k}, \omega) \right|^2 \phi_{pp}(\mathbf{k}, \omega) d\tilde{\mathbf{k}} d\mathbf{k} \right]. \quad (8)$$

$$\Pi_v^{\text{rad}}(\omega) = \text{Re} \left[\frac{\rho_a \omega}{16\pi^4} \int_{-\infty}^{\infty} \int_{-\infty}^{\infty} \frac{1}{\tilde{k}_z(\tilde{\mathbf{k}})} \left| \tilde{H}_v(\tilde{\mathbf{k}}, \mathbf{k}, \omega) \right|^2 \phi_{pp}(\mathbf{k}, \omega) d\tilde{\mathbf{k}} d\mathbf{k} \right]. \quad (9)$$

130 The subscripts $_p$ and $_v$ correspond to the formulations based on the pres-
 131 sure and velocity sensitivity functions, respectively. Considering that the
 132 $\phi_{pp}(\mathbf{k}, \omega)$ is always real, the only function which could make the integrand
 133 in Eqs. (8) and (9) complex is $\tilde{k}_z(\tilde{\mathbf{k}})$. According to Eq. (7), $\tilde{k}_z(\tilde{\mathbf{k}})$ becomes
 134 purely imaginary when the wavenumbers are outside the acoustic circle de-
 135 fined by $\Omega_a = \left\{ \tilde{\mathbf{k}} \in \mathbb{R}^2, |\tilde{\mathbf{k}}| \leq k_a \right\}$. Therefore, only wavenumbers inside the
 136 acoustic circle contribute to the radiated acoustic power. Hence, Eqs. (8)
 137 and (9) can be rewritten as

$$\Pi_p^{\text{rad}}(\omega) = \frac{1}{16\pi^4 \rho_a \omega} \int_{-\infty}^{\infty} \int_{\tilde{\mathbf{k}} \in \Omega_a} \sqrt{k_a^2 - \tilde{k}_x^2 - \tilde{k}_y^2} \left| \tilde{H}_p(\tilde{k}_x, \tilde{k}_y, \mathbf{k}, \omega) \right|^2 \phi_{pp}(\mathbf{k}, \omega) d\tilde{\mathbf{k}} d\mathbf{k}, \quad (10)$$

$$\Pi_v^{\text{rad}}(\omega) = \frac{\rho_a \omega}{16\pi^4} \int_{-\infty}^{\infty} \int_{\tilde{\mathbf{k}} \in \Omega_a} \frac{1}{\sqrt{k_a^2 - \tilde{k}_x^2 - \tilde{k}_y^2}} \left| \tilde{H}_v(\tilde{k}_x, \tilde{k}_y, \mathbf{k}, \omega) \right|^2 \phi_{pp}(\mathbf{k}, \omega) d\tilde{\mathbf{k}} d\mathbf{k}. \quad (11)$$

138 **3. Non-Negative Intensity**

139 In this section, an analytical formulation is presented for non-negative
 140 intensity (the active normal intensity) for planar structures under stochastic
 141 excitation to identify the areas of the vibrating structure that produce radia-
 142 tion to the far-field. The aim here is to develop a formula for $I^N(\mathbf{x}, \omega)$ which
 143 meets the two following conditions:

- 144 1. The NNI must be always non-negative. This will prevent acoustic short-
 145 circuit in the adjacent areas on the surface of the structure.
- 146 2. When integrating the NNI over the infinite boundary surface, it must
 147 produce the total sound power.

148 To meet the first condition, similar to works by Marburg et al. [8] and
 149 Williams [9] the NNI can be defined as follows

$$I^N(\mathbf{x}, \omega) = \frac{1}{4\pi^2} \int_{\infty} \beta(\mathbf{x}, \mathbf{k}, \omega) \beta^*(\mathbf{x}, \mathbf{k}, \omega) d\mathbf{k} = \frac{1}{4\pi^2} \int_{\infty} |\beta(\mathbf{x}, \mathbf{k}, \omega)|^2 d\mathbf{k}, \quad (12)$$

150 where $\beta(\mathbf{x}, \mathbf{k}, \omega)$ is a complex function which is not physically meaningful.
 151 It has been introduced in Eq. (12) to ensure that the NNI is always non-
 152 negative by definition. This satisfies the necessary condition for defining the
 153 NNI. The second condition for the NNI states that the total radiated acoustic
 154 power must be obtained by integrating the NNI over the infinite boundary
 155 surface

$$\Pi^{\text{rad}}(\omega) = \int_{\infty} I^N(\mathbf{x}, \omega) d\mathbf{x}. \quad (13)$$

156 Eq. (13) can be rewritten in terms of $\beta(\mathbf{x}, \mathbf{k}, \omega)$ as follows

$$\Pi^{\text{rad}}(\omega) = \frac{1}{4\pi^2} \int_{\infty} \int_{\infty} \beta(\mathbf{x}, \mathbf{k}, \omega) \beta^*(\mathbf{x}, \mathbf{k}, \omega) d\mathbf{k} d\mathbf{x} = \frac{1}{4\pi^2} \int_{\infty} \int_{\infty} |\beta(\mathbf{x}, \mathbf{k}, \omega)|^2 d\mathbf{k} d\mathbf{x}. \quad (14)$$

157 To meet the second condition, we propose two new formulae for $\beta(\mathbf{x}, \mathbf{k}, \omega)$,
 158 one in terms of pressure sensitivity function and the other one based on
 159 the sensitivity function of normal fluid particle velocity. Both formulae are

160 dependent on the CSD function of the stochastic field. The two formulae are
 161 given by

$$\beta_p(\mathbf{x}, \mathbf{k}, \omega) = \frac{\sqrt{\phi_{pp}(\mathbf{k}, \omega)}}{4\pi^2 \sqrt{\rho_a \omega}} \int_{\tilde{\mathbf{k}} \in \Omega_a} \sqrt[4]{k_a^2 - \tilde{k}_x^2 - \tilde{k}_y^2} \tilde{H}_p(\tilde{k}_x, \tilde{k}_y, \mathbf{k}, \omega) e^{i\tilde{\mathbf{k}}\mathbf{x}} d\tilde{\mathbf{k}}. \quad (15)$$

$$\beta_v(\mathbf{x}, \mathbf{k}, \omega) = \frac{\sqrt{\rho_a \omega \phi_{pp}(\mathbf{k}, \omega)}}{4\pi^2} \int_{\tilde{\mathbf{k}} \in \Omega_a} \frac{1}{\sqrt[4]{k_a^2 - \tilde{k}_x^2 - \tilde{k}_y^2}} \tilde{H}_v(\tilde{k}_x, \tilde{k}_y, \mathbf{k}, \omega) e^{i\tilde{\mathbf{k}}\mathbf{x}} d\tilde{\mathbf{k}}. \quad (16)$$

162 As can be seen from Eqs. (15) and (16), the integral domain is confined
 163 within the acoustic circle ($\tilde{\mathbf{k}} \in \Omega_a$) which means that $k_a^2 \geq \tilde{k}_x^2 + \tilde{k}_y^2$ and $\tilde{k}_z(\tilde{\mathbf{k}})$
 164 is real. These wavenumbers are associated with supersonic waves as their
 165 trace speeds are faster than the speed of sound. Whilst for the wavenumbers
 166 outside the acoustic circle, $\tilde{k}_z(\tilde{\mathbf{k}})$ is purely imaginary and the corresponding
 167 waves are called subsonic waves since they travel at phase speeds less than the
 168 speed of sound. The purpose of defining NNI is to identify local surfaces on
 169 a structure that are contributing to the far-field radiated sound. It is the far-
 170 field sound pressure that is normally of interest in engineering applications
 171 because this is the quantity to which a potential observer is typically exposed.
 172 The NNI enables the design engineers to identify the locations of unwanted
 173 sources of sound on the structure that make the most significant contributions
 174 to the far field. Therefore, only contributions of supersonic waves are taken
 175 into account and the subsonic components, which are evanescent and do not
 176 propagate to the far-field, are excluded.

177 To prove that the two formulae given by Eqs. (15) and (16) result in the
 178 radiated sound power as that given by Eqs. (10) and (11), Eq. (14) should
 179 be evaluated using Eqs. (15) and (16). In what follows, the proof is given for
 180 $\beta_v(\mathbf{k}, \omega)$ and similar approach can be used to verify that $\beta_p(\mathbf{k}, \omega)$ also meets
 181 this condition. $\beta_v^*(\mathbf{k}, \omega)$ can be written as follows

$$\beta_v^*(\mathbf{x}, \mathbf{k}, \omega) = \frac{\sqrt{\rho_a \omega \phi_{pp}(\mathbf{k}, \omega)}}{4\pi^2} \int_{\tilde{\mathbf{k}} \in \Omega_a} \frac{1}{\sqrt[4]{k_a^2 - \tilde{k}_x^2 - \tilde{k}_y^2}} \tilde{H}_v^*(\tilde{k}_x, \tilde{k}_y, \mathbf{k}, \omega) e^{-i\tilde{\mathbf{k}}\mathbf{x}} d\tilde{\mathbf{k}}, \quad (17)$$

182 substituting Eqs. (16) and (17) into Eq. (14)

$$\Pi_v^{\text{rad}}(\omega) = \frac{\rho_a \omega}{16\pi^4} \int_{\infty} \int_{\tilde{\mathbf{k}} \in \Omega_a} \int_{\tilde{\mathbf{k}} \in \Omega_a} \frac{\tilde{H}_v(\tilde{k}_x, \tilde{k}_y, \mathbf{k}, \omega) \tilde{H}_v^*(\tilde{k}_x, \tilde{k}_y, \mathbf{k}, \omega)}{\sqrt[4]{k_a^2 - \tilde{k}_x^2 - \tilde{k}_y^2} \sqrt[4]{k_a^2 - \tilde{k}_x^2 - \tilde{k}_y^2}} d\tilde{\mathbf{k}} \quad (18)$$

$$\left(\frac{1}{4\pi^2} \int_{\infty} e^{i(\tilde{\mathbf{k}} - \tilde{\mathbf{k}})\mathbf{x}} d\mathbf{x} \right) d\tilde{\mathbf{k}} \phi_{pp}(\mathbf{k}, \omega) d\mathbf{k},$$

using the integral in the parenthesis in Eq. (18) corresponds to the Dirac delta function which is given by [27]

$$\frac{1}{4\pi^2} \int_{\infty} e^{i(\tilde{\mathbf{k}} - \tilde{\mathbf{k}})\mathbf{x}} d\mathbf{x} = \delta(\tilde{\mathbf{k}} - \tilde{\mathbf{k}}), \quad (19)$$

183 using this definition, Eq. (18) can be simplified to

$$\Pi_v^{\text{rad}}(\omega) = \frac{\rho_a \omega}{16\pi^4} \int_{\infty} \int_{\tilde{\mathbf{k}} \in \Omega_a} \frac{1}{\sqrt{k_a^2 - \tilde{k}_x^2 - \tilde{k}_y^2}} \left| \tilde{H}_v(\tilde{k}_x, \tilde{k}_y, \mathbf{k}, \omega) \right|^2 \phi_{pp}(\mathbf{k}, \omega) d\tilde{\mathbf{k}} d\mathbf{k}. \quad (20)$$

184 This equation is exactly the same as Eq. (11). The NNI formulae can be
185 obtained by substituting Eqs. (15) and (16) into Eq. (12)

$$I_p^N(\mathbf{x}, \omega) = \frac{1}{(4\pi^2)^3 \rho_a \omega} \int_{\infty} \left| \int_{\tilde{\mathbf{k}} \in \Omega_a} \sqrt[4]{k_a^2 - \tilde{k}_x^2 - \tilde{k}_y^2} \tilde{H}_p(\tilde{k}_x, \tilde{k}_y, \mathbf{k}, \omega) e^{i\tilde{\mathbf{k}}\mathbf{x}} d\tilde{\mathbf{k}} \right|^2 |\phi_{pp}(\mathbf{k}, \omega)| d\mathbf{k}, \quad (21)$$

$$I_v^N(\mathbf{x}, \omega) = \frac{\rho_a \omega}{(4\pi^2)^3} \int_{\infty} \left| \int_{\tilde{\mathbf{k}} \in \Omega_a} \frac{1}{\sqrt[4]{k_a^2 - \tilde{k}_x^2 - \tilde{k}_y^2}} \tilde{H}_v(\tilde{k}_x, \tilde{k}_y, \mathbf{k}, \omega) e^{i\tilde{\mathbf{k}}\mathbf{x}} d\tilde{\mathbf{k}} \right|^2 |\phi_{pp}(\mathbf{k}, \omega)| d\mathbf{k}. \quad (22)$$

186 Due to the magnitude operation, these formulae are guaranteed to yield non-
187 negative results.

188 In Eq. (22), the term in the denominator tends to zero for the wavenum-
189 bers on the acoustic circle. Generally, singular integrals can be numerically

190 evaluated as described in Refs [28; 29]. However, Singularity in Eq. (22) can
 191 be analytically removed using the following conversion formulae

$$\tilde{k}_x = \tilde{k}_r \cos\theta; \quad \tilde{k}_y = \tilde{k}_r \sin\theta, \quad (23)$$

192 Eq. (22) can then be transformed to polar wavenumber coordinates as follows

$$I_v^N(\mathbf{x}, \omega) = \frac{\rho_a \omega}{(4\pi^2)^3} \int_{-\infty}^{\infty} \left| \left(\int_{\theta=0}^{\theta=2\pi} \int_{\tilde{k}_r=0}^{\tilde{k}_r=k_a} \frac{\tilde{k}_r}{\sqrt[4]{k_a^2 - \tilde{k}_r^2}} \right. \right. \quad (24)$$

$$\left. \left. \tilde{H}_v(\tilde{k}_r \cos\theta, \tilde{k}_r \sin\theta, \mathbf{k}, \omega) e^{i\tilde{k}_r(x\cos\theta + y\sin\theta)} d\tilde{k}_r d\theta \right) \right|^2 |\phi_{pp}(\mathbf{k}, \omega)| d\mathbf{k}.$$

193 Finally, the change of variable, $\tilde{k}_r = k_a \sin\gamma$ analytically removes the singu-
 194 larity from the integral. As such, Eq. (24) can be expressed by

$$I_v^N(\mathbf{x}, \omega) = \frac{\rho_a \omega k_a^3}{(4\pi^2)^3} \int_{-\infty}^{\infty} \left| \left(\int_{\theta=0}^{\theta=2\pi} \int_{\gamma=0}^{\gamma=\frac{\pi}{2}} \sin\gamma \sqrt{\cos\gamma} e^{ik_a \sin\gamma(x\cos\theta + y\sin\theta)} \right. \right. \quad (25)$$

$$\left. \left. \tilde{H}_v(k_a \sin\gamma \cos\theta, k_a \sin\gamma \sin\theta, \mathbf{k}, \omega) d\gamma d\theta \right) \right|^2 |\phi_{pp}(\mathbf{k}, \omega)| d\mathbf{k},$$

195 the rectangular method for the numerical integration in Eqs. (25) and (21),
 196 the NNI becomes

$$I_v^N(\mathbf{x}, \omega) = \frac{\rho_a \omega k_a^3}{(4\pi^2)^3} \sum_{\mathbf{k} \in \Omega_t} \left| \left(\sum_{\theta \in [0, 2\pi]} \sum_{\gamma \in [0, \frac{\pi}{2}]} \sin\gamma \sqrt{\cos\gamma} e^{ik_a \sin\gamma(x\cos\theta + y\sin\theta)} \right. \right. \quad (26)$$

$$\left. \left. \tilde{H}_v(k_a \sin\gamma \cos\theta, k_a \sin\gamma \sin\theta, \mathbf{k}, \omega) \delta\gamma \delta\theta \right) \right|^2 |\phi_{pp}(\mathbf{k}, \omega)| d\mathbf{k},$$

197

$$I_p^N(\mathbf{x}, \omega) = \frac{1}{(4\pi^2)^3 \rho_a \omega} \sum_{\mathbf{k} \in \Omega_t} \left| \left(\sum_{\tilde{\mathbf{k}} \in \Omega_a} \sqrt[4]{k_a^2 - \tilde{k}_x^2 - \tilde{k}_y^2} \tilde{H}_p(\tilde{k}_x, \tilde{k}_y, \mathbf{k}, \omega) e^{i\tilde{\mathbf{k}}\mathbf{x}} \delta\tilde{\mathbf{k}} \right) \right|^2 \quad (27)$$

$$|\phi_{pp}(\mathbf{k}, \omega)| \delta\mathbf{k}.$$

198 Ω_t is a truncated wavenumber domain and $\delta\gamma$, $\delta\theta$, $\delta\mathbf{k}$ and $\delta\tilde{\mathbf{k}}$ are the in-
 199 crements in the numerical integration. For the ADF excitation, since the

200 normalized CSD function $\tilde{\phi}_{pp}^{\text{ADF}}(k_x, k_y, \omega)$ is null for the wavenumbers larger
 201 than the acoustic wavenumber, the truncated wavenumber domain is basi-
 202 cally the acoustic circle Ω_a .

203 It is also noteworthy that the NNI formulae expressed by Eqs. (26) and
 204 (27) can be used for both infinite planar structure and finite plate in an infi-
 205 nite baffle. To compute the NNI, one requires determination of the sensitivity
 206 functions. The sensitivity functions can be either calculated analytically or
 207 numerically. For example, the finite element method can be employed to
 208 obtain the sensitivity functions. In the following section, the NNI formula-
 209 tion is applied to a finite baffled panel for which the sensitivity functions are
 210 analytically determined.

211 4. Application to Rectangular Baffled Panels

212 A rectangular baffled panel excited by a stochastic pressure field is shown
 213 in Figure 1. The spatial average of the auto spectrum density (ASD) of the
 214 panel velocity is given by [30–32]

$$S_{vv}(\mathbf{x}, \omega) = \frac{1}{4\pi^2} \int_{\infty} |H_{vs}(\mathbf{x}, \mathbf{k}, \omega)|^2 \phi_{pp}(\mathbf{k}, \omega) d\mathbf{k}, \quad (28)$$

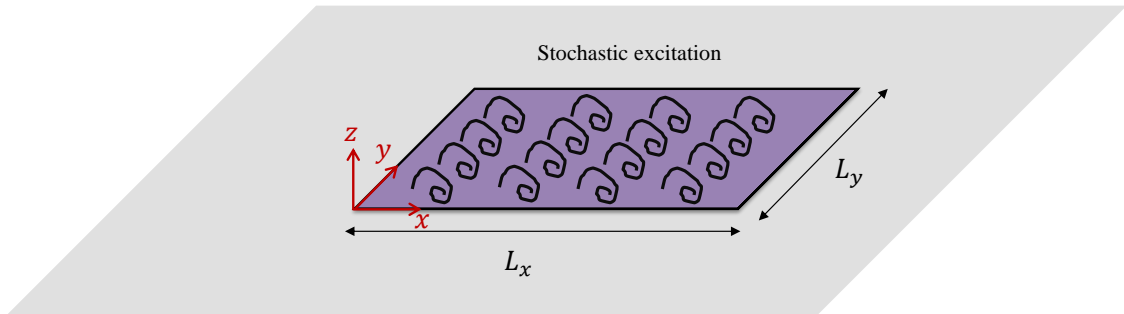


Figure 1: A baffled panel under stochastic excitation.

215 where $H_{vs}(\mathbf{x}, \mathbf{k}, \omega)$ is the sensitivity function of the panel velocity excited by
 216 a unit wall plane wave. The spatial average of the ASD of the panel velocity

217 is given by

$$\langle V^2 \rangle = \frac{1}{A} \int_A S_{vv}(\mathbf{x}, \omega) dA, \quad (29)$$

218 $A = L_x L_y$ is the panel surface area and L_x, L_y are the panel length and width
 219 in the x and y directions, respectively. Eqs. (28) and (29) can be evaluated
 220 using rectangular method as described in Ref [32]

The ASD of the radiated pressure from the panel excited by the stochastic field is also given by

$$S_{pp}(\mathbf{x}, \omega) = \frac{1}{4\pi^2} \int_{-\infty}^{\infty} |H_p(\mathbf{x}, \mathbf{k}, \omega)|^2 \phi_{pp}(\mathbf{k}, \omega) d\mathbf{k}, \quad (30)$$

221 assuming that CSD of the stochastic field is known, it can be seen from
 222 the equations in Sections 2-4 that to evaluate $\Pi^{\text{rad}}, I_{\text{act}}, I^N, S_{vv}$ and S_{pp} ,
 223 the sensitivity functions of panel velocity, normal fluid particle velocity and
 224 radiated pressure have to be known. In what follows, determination of these
 225 sensitivity functions are discussed.

226 4.1. Determination of the Sensitivity Functions

For a simply supported rectangular panel excited by a unit wall plane wave, the sensitivity function $H_{v_s}(\mathbf{x}, \mathbf{k}, \omega)$ corresponding to the velocity at point \mathbf{x} is given by [32]

$$H_{v_s}(\mathbf{x}, \mathbf{k}, \omega) = i\omega \sum_{m=1}^M \sum_{n=1}^N \frac{\psi_{mn}(\mathbf{k}) \varphi_{mn}(\mathbf{x})}{\Omega(\omega_{mn}^2 - \omega^2 + i\eta\omega\omega_{mn})}, \quad (31)$$

$\Omega = \rho_s h L_x L_y / 4$ is the modal mass. The modal frequencies are given by

$$\omega_{mn} = \sqrt{\frac{D}{\rho_s h} \left(\left(\frac{m\pi}{L_x} \right)^2 + \left(\frac{n\pi}{L_y} \right)^2 \right)}, \quad (32)$$

where $D = Eh^3/(12(1-\nu^2))$ is the flexural rigidity, E is the Young's modulus and ν is Poisson's ratio. The modal forces ψ_{mn} are calculated by integration over the panel surface as follows

$$\psi_{mn}(\mathbf{k}) = \int_A \varphi_{mn}(\mathbf{x}) e^{-i(k_x x + k_y y)} dA = I_m^x(k_x) I_n^y(k_y), \quad (33)$$

where $\varphi_{mn}(\mathbf{x})$ are the panel mode shapes given by

$$\varphi_{mn}(\mathbf{x}) = \sin\left(\frac{m\pi x}{L_x}\right) \sin\left(\frac{n\pi y}{L_y}\right), \quad (34)$$

227 and

$$\{I_s^r(k_r)|(r, s) = (x, m) \vee (y, n)\} = \left\{ \begin{array}{ll} \left(\frac{s\pi}{L_r}\right) \frac{(-1)^s e^{-i(k_r L_r)} - 1}{k_r^2 - \left(\frac{s\pi}{L_r}\right)^2}, & k_r \neq \frac{s\pi}{L_r} \\ \frac{1}{2}iL_r, & \text{otherwise} \end{array} \right\}. \quad (35)$$

228 At the interface between the panel and the acoustic domain, the structural
 229 velocity v_s is equal to fluid particle velocity v in the normal direction, that
 230 is $H_v(\mathbf{x}, \mathbf{k}, \omega) = H_{v_s}(\mathbf{x}, \mathbf{k}, \omega)$. As such, the spectral sensitivity function of
 231 normal fluid particle velocity $\tilde{H}_v(\tilde{\mathbf{k}}, \mathbf{k}, \omega)$ can be obtained analytically using
 232 a Fourier transform as follows

$$\tilde{H}_v(\tilde{\mathbf{k}}, \mathbf{k}, \omega) = \int_{-\infty}^{\infty} H_v(\mathbf{x}, \mathbf{k}, \omega) e^{-i\tilde{\mathbf{k}}\mathbf{x}} d\mathbf{x} = \sum_{m=1}^M \sum_{n=1}^N a_{mn}(\tilde{\mathbf{k}}, \omega) \psi_{mn}(\mathbf{k}), \quad (36)$$

233 where

$$a_{mn}(\tilde{\mathbf{k}}, \omega) = i\omega \frac{\psi_{mn}(\tilde{\mathbf{k}})}{\Omega(\omega_{mn}^2 - \omega^2 + i\eta\omega\omega_{mn})}, \quad (37)$$

234 and ψ_{mn} and I_s^r are given by Eqs. (33)-(35).

235 Since $\tilde{H}_p(\tilde{\mathbf{k}}, \mathbf{k}, \omega)$ is related to $\tilde{H}_v(\tilde{\mathbf{k}}, \mathbf{k}, \omega)$ by Eq. (6), to obtain $H_p(\mathbf{x}, \mathbf{k}, \omega)$,
 236 one can compute the inverse Fourier transform of Eq. (6). However, in order
 237 to avoid an additional inverse Fourier transform we used an alternative
 238 approach based on the Lyamshev reciprocity principle [33; 34]. Figure 2
 239 illustrates the Lyamshev reciprocity principle for a baffled panel.

According to Lyamshev reciprocity principle, the ratio of the pressure at
 point \mathbf{x} over the applied normal force at point \mathbf{x}' is equal to the ratio of the
 normal velocity of the panel at point \mathbf{x}' over the volume velocity Q_v of a
 monopole source placed at point \mathbf{x} , that is,

$$H_{p/F}(\mathbf{x}, \mathbf{x}', \omega) = H_{v/Q_v}(\mathbf{x}', \mathbf{x}, \omega), \quad (38)$$

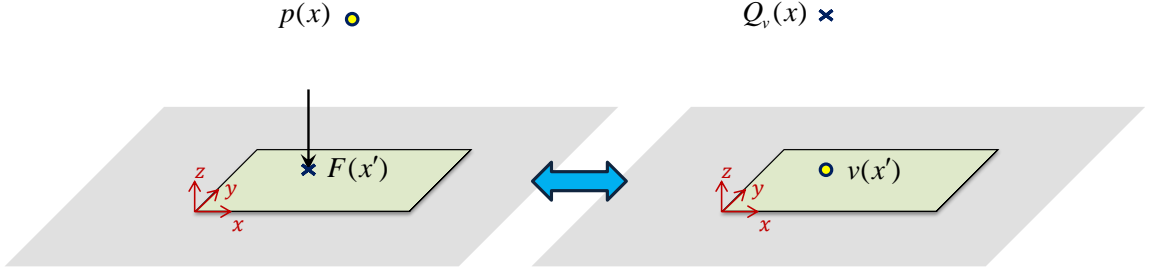


Figure 2: Illustration of the Lyamshev reciprocity principle for a baffled panel.

where

$$H_{v/Q_v}(\mathbf{x}', \mathbf{x}, \omega) = i\omega \sum_{m=1}^M \sum_{n=1}^N \frac{F_{mn}(\mathbf{x}) \varphi_{mn}(\mathbf{x}')}{\Omega(\omega_{mn}^2 - \omega^2 + i\eta\omega\omega_{mn})}, \quad (39)$$

and

$$F_{mn}(\mathbf{x}) = \int_A p(\mathbf{x}, \mathbf{x}', \omega) \varphi_{mn}(\mathbf{x}') d\mathbf{x}', \quad (40)$$

where $p(\mathbf{x}, \mathbf{x}', \omega)$ is the acoustic pressure generated by a monopole source and is given by

$$p(\mathbf{x}, \mathbf{x}', \omega) = \frac{i\rho_a\omega Q_v}{2\pi\mathbf{r}} e^{-ik_a\mathbf{r}}, \quad \mathbf{r} = |\mathbf{x} - \mathbf{x}'|. \quad (41)$$

The sensitivity function of the radiated pressure is given by

$$H_p(\mathbf{x}, \mathbf{k}, \omega) = \int_{\infty} H_{p/F}(\mathbf{x}, \mathbf{x}', \omega) e^{-i\mathbf{k}\mathbf{x}'} d\mathbf{x}', \quad (42)$$

substituting Eqs. (38)-(39) into Eq. (42), the sensitivity function $H_p(\mathbf{x}, \mathbf{k}, \omega)$ can be written as follows

$$H_p(\mathbf{x}, \mathbf{k}, \omega) = \sum_{m=1}^M \sum_{n=1}^N a_{mn}(\mathbf{k}, \omega) F_{mn}(\mathbf{x}), \quad (43)$$

240 where $F_{mn}(\mathbf{x})$ is given by Eq. (40) and can be numerically computed using
 241 rectangular method.

Table 1. Dimensions and material properties of the panel

Parameter	Value
Young's modulus, E (GPa)	70
Poisson's ratio, ν	0.3
Mass density, ρ_s (kg/m ³)	2700
Length, L_x (mm)	480
Width, L_y (mm)	420
Thickness, h_s (mm)	3.17
Damping loss factor, η	0.005

242 **5. Results and Discussion**

243 A rectangular baffled panel with simply-supported boundary conditions
 244 is considered. The dimensions and material properties of the panel are listed
 245 in Table 1. The fluid density and kinematic viscosity were set to 1.225 kg/m³
 246 and 1.511×10^{-5} m²/s, respectively.

247

248 *5.1. Modeling TBL and ADF Excitations*

249 The surface contributions of the panel to the radiated sound power under
 250 two different stochastic excitations, namely TBL and ADF are examined.
 251 The CSD of the stochastic field can be expressed in terms of the ASD function
 252 $\Psi_{pp}(\omega)$ and the normalized CSD function of the stochastic field $\tilde{\phi}_{pp}(\mathbf{k}, \omega)$ as
 253 follows [35; 36]

$$\phi_{pp}(\mathbf{k}, \omega) = \Psi_{pp}(\omega)\tilde{\phi}_{pp}(\mathbf{k}, \omega). \quad (44)$$

Eq. (44) can be used to evaluate the CSD of both the ADF and TBL excitations. A unity ASD is assumed for both excitations. The normalized CSD functions given in Appendix A were also used to evaluate the TBL and ADF excitations, respectively. For TBL excitation, it is assumed that the TBL is stationary, homogeneous and fully developed over the panel surface. Moreover, it is assumed the vibration of the panel does not alter the wall pressure field (WPF). The Mellen model described in Appendix A was used to evaluate the CSD function of the WPF [37]. The TBL parameters were estimated based on theoretical formula for a flat panel from literature and are given in Table 2 [32]. The convective velocity U_c was approximated as follows [32; 38]

$$U_c \cong U_\infty(0.59 + 0.3e^{-0.89\delta^*\omega/U_\infty}), \quad (45)$$

Table 2. TBL parameters at a flow speed of 40 m/s

Parameter	Value
TBL thickness δ (m)	0.0349
TBL displacement thickness δ^* (m)	0.0044
Wall shear stress τ (Pa)	2.5228

254 where U_∞ is the free flow velocity and δ^* is boundary layer displacement
 255 thickness.

256

257 5.2. Determination of Cut-off Wavenumbers and Wavenumber Resolutions

258 It has previously been reported when a panel is excited by a TBL, the
 259 effect of convected ridge can be neglected for frequencies well above the aero-
 260 dynamic frequency [26; 32]. Therefore, to predict the vibroacoustic response
 261 of the panel the cut-off wavenumber can be defined based on the flexural
 262 wavenumber. This is due to the filtering effect of the structure. In this
 263 study, it was confirmed that the same criterion can be used to evaluate the
 264 NNI. One can plot the forcing function and sensitivity function to illustrate
 265 the filtering effect. To do this, Eq. (22) can be further written in a compact
 266 form as follows

$$I_v^N(\mathbf{x}, \omega) = \left(\frac{1}{4\pi^2} \right) \int_{\infty} \left| \tilde{H}_N(\mathbf{x}, \mathbf{k}, \omega) \right|^2 \phi_{pp}(\mathbf{k}, \omega) d\mathbf{k}, \quad (46)$$

267 where $\tilde{H}_N(\mathbf{x}, \mathbf{k}, \omega)$ is the NNI sensitivity function given by

$$\tilde{H}_N(\mathbf{x}, \mathbf{k}, \omega) = \frac{\sqrt{\rho_a \omega k_a^3}}{4\pi^2} \left(\sum_{\theta \in [0, 2\pi]} \sum_{\gamma \in [0, \frac{\pi}{2}]} \sin \gamma \sqrt{\cos \gamma} e^{ik_a \sin \gamma (x \cos \theta + y \sin \theta)} \right. \\ \left. \tilde{H}_v(k_a \sin \gamma \cos \theta, k_a \sin \gamma \sin \theta, \mathbf{k}, \omega) \delta \gamma \delta \theta \right) \quad (47)$$

268 Figure 3(a) presents a map of the NNI sensitivity function at $(x, y) =$
 269 $(0.4 \text{ m}, 0.4 \text{ m})$ and for $k_y = 0$. The black dashed lines correspond to the
 270 panel flexural wavenumbers. It can be seen that the sensitivity function
 271 reaches its maximum values at wavenumbers smaller than or close to the flex-
 272 ural wavenumbers. However, for the wavenumbers larger than the flexural
 273 wavenumbers the magnitude of the function is still considerable, particularly

274 at resonance frequencies. Figure 3(b) shows the TBL forcing function, corre-
 275 sponding to the CSD of the WPF. The convective wavenumbers are denoted
 276 by the dash-dotted line. Figure 3(c) presents the product of the sensitivity
 277 function and forcing function. It can be observed from Figure 3(c) that most
 278 of the wavenumbers larger than flexural wavenumber are filtered out. There-
 279 fore, only wavenumbers smaller than flexural wavenumbers contribute to the
 280 NNI. However, a small effect of the convective ridge on the product of the
 281 sensitivity function and forcing function can be observed around 150 Hz and
 282 350 Hz. Whilst this contribution is not significant, the effect of the convective
 283 ridge was taken into account here as the cut-off wavenumber was defined as
 284 twice the flexural wavenumber at the highest frequency of interest. In fact, a
 285 cut-off wavenumber of $k_{\text{cut-off}} = 2k_{p,\text{max}}$ was selected. Therefore, a wavenum-
 286 ber range of $[-2k_{p,\text{max}}, 2k_{p,\text{max}}]$ was used in both the streamwise and spanwise
 287 directions where $k_{p,\text{max}} = (\omega_{\text{max}} \sqrt{\rho_s h / D})^{1/2}$ is the flexural wavenumber of the
 288 panel at the maximum frequency of interest denoted by ω_{max} . The wavenum-
 289 ber resolutions were set to $\delta k_x = \delta k_y = 0.25$ (1/m), and $\delta \gamma$, $\delta \theta$ were set to
 290 $\pi/60$. These values were determined using a convergence study. It should
 291 also be pointed out that although the NNI sensitivity function was plotted
 292 at a certain point on the panel, the same filtering effect occurs for all the
 293 points on the panel and similar behavior could be observed if the maps were
 294 plotted at a different point.

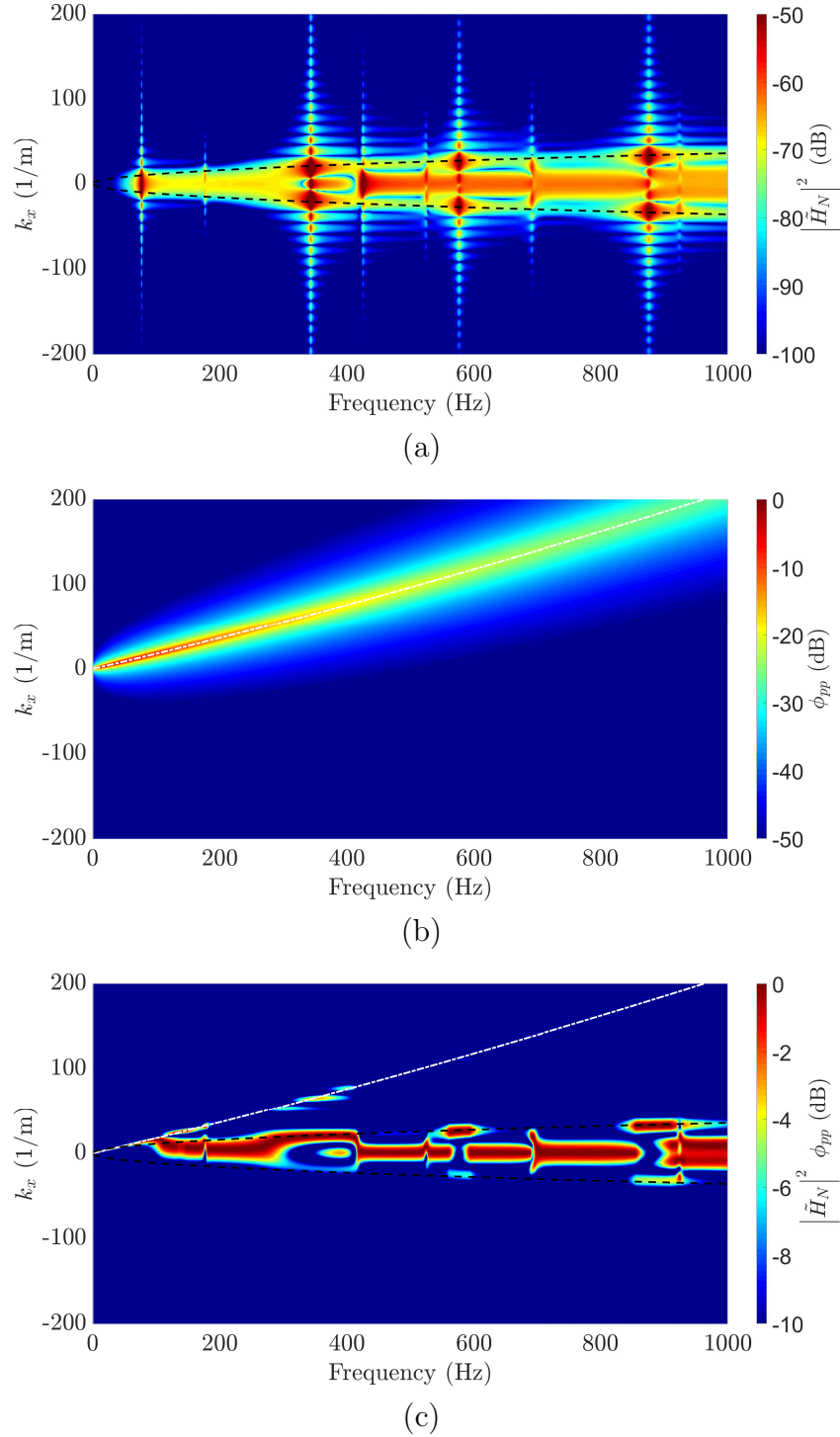


Figure 3: Maps of the (a) NNI sensitivity functions $\left| \tilde{H}_N(\mathbf{x}, \mathbf{k}, \omega) \right|^2$ (dB, ref. $\text{Pa}^{-1}\text{m}^3\text{s}^{-2}\text{rad}^2$), (b) CSD function of the wall pressure spectrum using the Mellen model $\phi_{pp}(\mathbf{k}, \omega)$ (dB, ref. $1 \text{ Pa}^2\text{m}^2\text{s rad}^{-2}$), and (c) result obtained by the product of (a) and (b) normalized by the maximum value at each frequency (dB, ref. 1 Wm^2). The black dashed lines in (a) and (c) correspond to the panel flexural wavenumber; the white dashed-dot line in (b) and (c) corresponds to the convective wavenumber.

295 *5.3. Vibroacoustic Response of the Panel*

296 Figures 4 and 5 respectively present the spatial average of the ASD of
 297 the panel velocity and the radiated sound power of the panel under the TBL
 298 and ADF excitations. The TBL excitation strongly excites the structure
 299 at the aerodynamic coincidence frequency, f_c , which occurs when the flex-
 300 ural wavenumber given by $k_p = (\omega\sqrt{\rho_s h/D})^{1/2}$ is equal to the convective
 301 wavenumber $k_c = \omega/U_c$, that is, $f_c = U_c^2\sqrt{\rho_s h/D}/(2\pi)$ [39]. For the param-
 302 eters chosen here and at a flow speed of 40 m/s, $f_c=29$ Hz. It can be seen
 303 from both figures that except at very low frequencies the spectral levels of
 304 the velocity and the sound power of the panel under the ADF excitation are
 305 significantly higher than those for the panel excited by the TBL (a unity
 306 ASD of the stochastic field was assumed for both excitations). Further, the
 307 shape and trend of the panel velocity response under the TBL excitation is
 308 very similar to that under the ADF excitation. However, a different behav-
 309 ior for the radiated sound power can be observed in Figure 5. The radiated
 310 sound power between resonance frequencies for the ADF excitation is rela-
 311 tively flat whilst the sound power at those frequencies form a curved shape
 312 in the spectra for the TBL excitation.

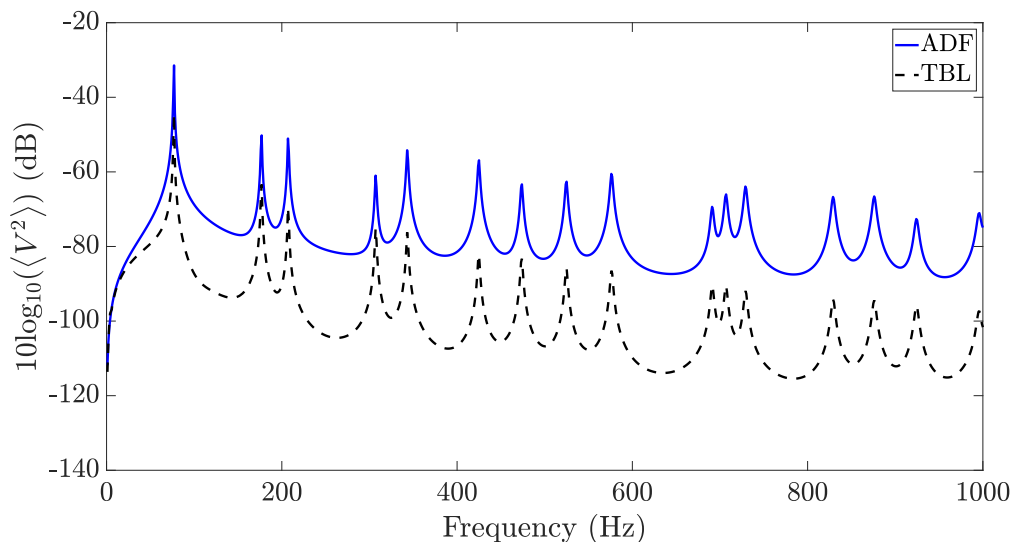


Figure 4: Predicted mean quadratic velocity spectra for the TBL and ADF excitations (dB ref. 1 (m/s)²/Hz).

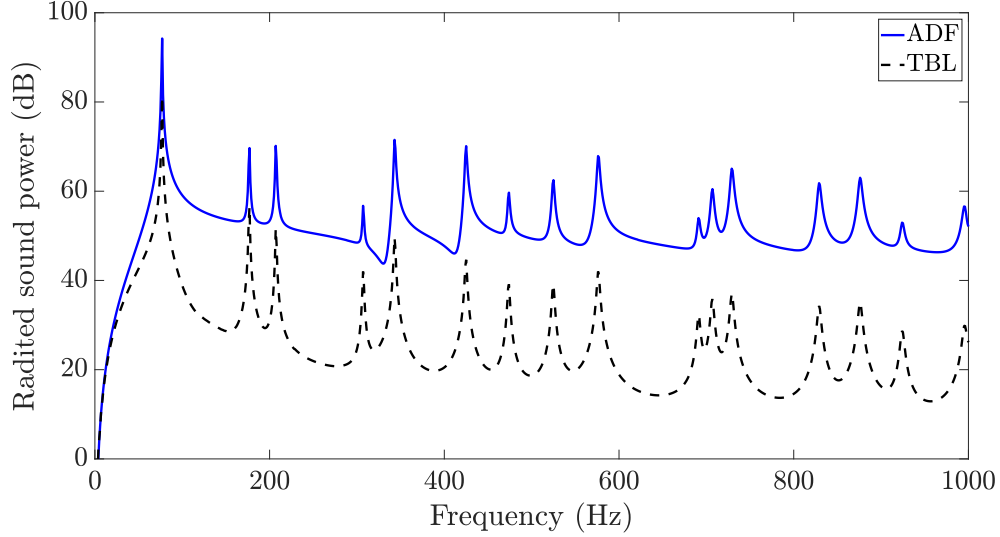


Figure 5: Predicted acoustic power of the panel under the TBL and ADF excitations (dB ref. 1×10^{-12} (W)).

Figure 6 shows the radiation efficiency of the panel for both the ADF and TBL excitations. The radiation efficiency of a panel is given by [40]

$$\sigma = \frac{\Pi_{\text{rad}}}{A\rho_a c_a \langle V^2 \rangle}, \quad (48)$$

313 vertical lines in Figure 6 indicate the resonance frequencies of the panel, the
 314 mode number for each resonance frequency has also been shown ((m, n) mode
 315 means an m mode in the x -direction and an n mode in the y -direction). It
 316 can be observed from Figure 6 that at very low frequencies the radiation
 317 efficiency of the panel is independent of the excitation force, and at higher
 318 frequencies the radiation efficiency of the panel under the ADF excitation
 319 is generally higher than that of the panel excited by the TBL, particularly
 320 at non-resonance frequency, the ADF excited panel efficiently radiates sound
 321 to the acoustic domain. At resonance frequency, the radiation frequency is
 322 almost the same for both excitations.

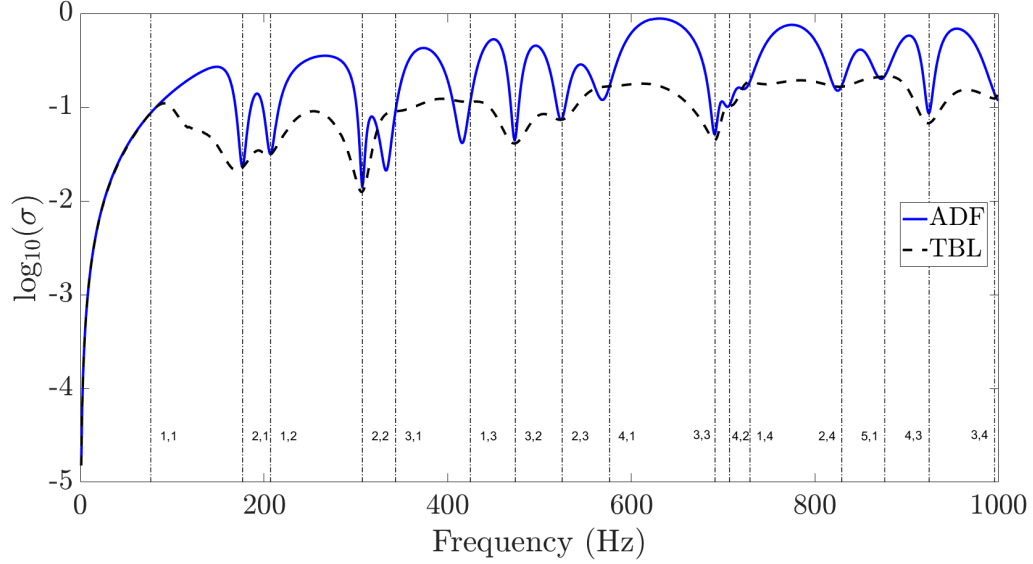


Figure 6: Radiation efficiency of the panel under the TBL and ADF excitations.

323 *5.4. The NNI Calculation*

324 To identify the surface contributions of the panel to the radiated sound
 325 power under the ADF and TBL excitations, the NNI has been computed at
 326 four discrete resonance frequencies of 177 Hz, 307 Hz, 691 Hz and 924 Hz as
 327 well as at two non-resonance frequencies of 630 Hz and 700 Hz. The maps
 328 of S_{vv} , S_{pp} , I_{act} and I^N at the selected frequencies are presented in Figures 7
 329 and 8 for the panel under the TBL and ADF excitations, respectively. It can
 330 be observed that regardless of excitation, at each frequency (particularly at
 331 the resonance frequencies) the map of S_{vv} is very similar to that of S_{pp} . This
 332 is not surprising as S_{pp} was evaluated on the surface of the panel, and the
 333 sensitivity functions of velocity and pressure have similar characteristic and
 334 are related to each other by Eq. (6). Figures 7 and 8 show that the active
 335 normal intensity I_{act} of the panel excited by the ADF is higher than that
 336 under the TBL excitation, this is consistent with the sound power results
 337 presented in Figure 5. Further, it can be seen that the maps of I_{act} for both
 338 excitations are very similar and the patterns at the resonance frequencies are
 339 highly dominated by the mode shapes.

340 For the TBL excitation, the NNI shows a distribution where mainly the
 341 edges and corners of the panel are significantly contributing to the radiated
 342 sound. This is consistent with the concept of edge and corner modes

343 introduced by Maidanik [41]. For example, at 177 Hz the edge mode is con-
 344 tributing to the far-field sound power while at 307 Hz, 691 Hz, 700 Hz and
 345 924 Hz the corner modes are the main contributor. At 630 Hz, a large surface
 346 located between the center and two edges of the panel generates propagative
 347 waves to the far field. For the ADF excitation at 177 Hz and 924 Hz a similar
 348 NNI distribution to those of TBL excitation in Figure 7 can be observed. At
 349 these two resonance frequencies, regardless of excitation, only edge and cor-
 350 ner modes are contributing to the radiated sound. Figures 7 and 8 show that
 351 the NNI distribution for the panel under the TBL excitation at 307 Hz and
 352 700 Hz are mainly at the corners of the panel while for the ADF excitation
 353 the NNI is distributed along the diagonal of the panel with high intensity in
 354 the middle of the panel. Further, at 630 Hz the hot spots are formed as two
 355 separate vertical ellipses for the TBL excited panel while for the ADF excited
 356 panel the NNI was contained within a large horizontal ellipse. According to
 357 Figures 7 and 8, in addition to the corner modes which effectively generate
 358 supersonic waves to the far field for both excitations at 691 Hz, there is a
 359 hot spot in the middle of the panel for the ADF excitation which radiates
 360 energy to the far field. Results in Figures 7 and 8 revealed that the NNI
 361 distribution depends on the excitation type and frequency.

362 It should be noted that since normal fluid particle velocity is zero over
 363 the baffle (outside the panel surface), the active normal intensity is also zero
 364 everywhere on the baffle. Therefore, plotting I_{act} over the panel surface
 365 shows the total intensity pattern, and the total radiated sound power can be
 366 evaluated by taking the integral of I_{act} over the panel surface. However, the
 367 NNI is not necessarily zero on the baffle. To obtain the total sound power
 368 from the NNI, its entire distribution over the infinite boundary surface has to
 369 be considered as indicated by Eq. (13). Hence, the whole NNI distributions
 370 are plotted over a large boundary surface at $z = 0$ for the selected frequencies
 371 as shown in Figures 9 and 10. The solid white lines in the maps indicate
 372 the rectangular panel under ADF/TBL excitations. Figures 9 and 10 show
 373 that the maxima of the NNI are usually located outside the panel surface,
 374 particularly at low frequencies as shown in Figure 9(a) and (b). The NNI
 375 distributions shown in Figures 7 and 8 are basically small parts of the whole
 376 distributions at most selected frequencies. The total NNI distribution in
 377 Figures 9 and 10 can be considered as an image of the excitation sources
 378 viewed by the acoustic domain. For instance, Figure 9 shows that at 177 Hz
 379 the size of each hot spot is around 1 m which corresponds to the half acoustic
 380 wavelength. Hence, the spatial resolution of the NNI is directly related to

381 the acoustic wavelength.

382 As can be seen in Figure 9(c) almost the whole area of the panel under
 383 the ADF excitation is contributing to the radiated sound. At this frequency
 384 a high radiation is expected, this is consistent with the results in Figure 6
 385 where the radiation efficiency of the panel is close to 100 % (i.e. $\sigma = 1$) at
 386 630 Hz . From the maps of the NNI at the peaks of the radiation efficiency
 387 (results are not shown here), it was confirmed that concentration of the NNI
 388 distribution within the panel surface results in high radiation efficiency of the
 389 panel under the ADF/TBL excitations. The formulation derived here can
 390 be applied to identify hot spots of a structure under stochastic excitations.
 391 Further, it can give an insight into the radiation efficiency of the structure
 392 based on the NNI distribution over the structural-acoustic boundary surface.

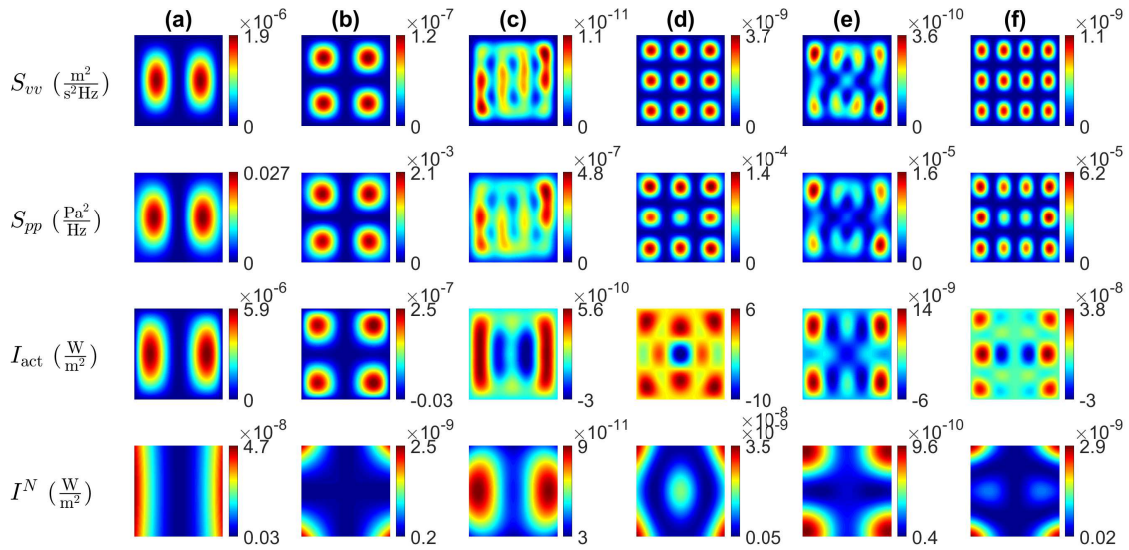


Figure 7: Maps of S_{vv} , S_{pp} , I_{act} and I^N for the panel under the TBL excitation at a flow velocity of $U_\infty = 40$ m/s and at selected frequencies of (a) 177 Hz, (b) 307 Hz, (c) 630 Hz, (d) 691 Hz, (e) 700 Hz and (f) 924 Hz.

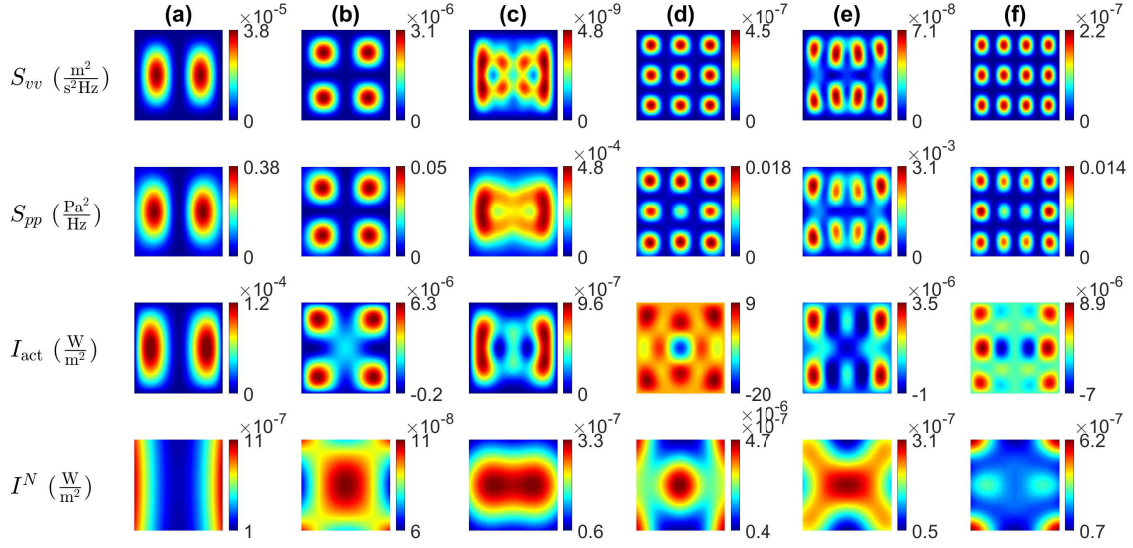


Figure 8: Maps of S_{vv} , S_{pp} , I_{act} and I^N for the panel under ADF excitation at a flow velocity of $U_\infty = 40$ m/s and at selected frequencies of (a) 177 Hz, (b) 307 Hz, (c) 630 Hz, (d) 691 Hz, (e) 700 Hz and (f) 924 Hz.

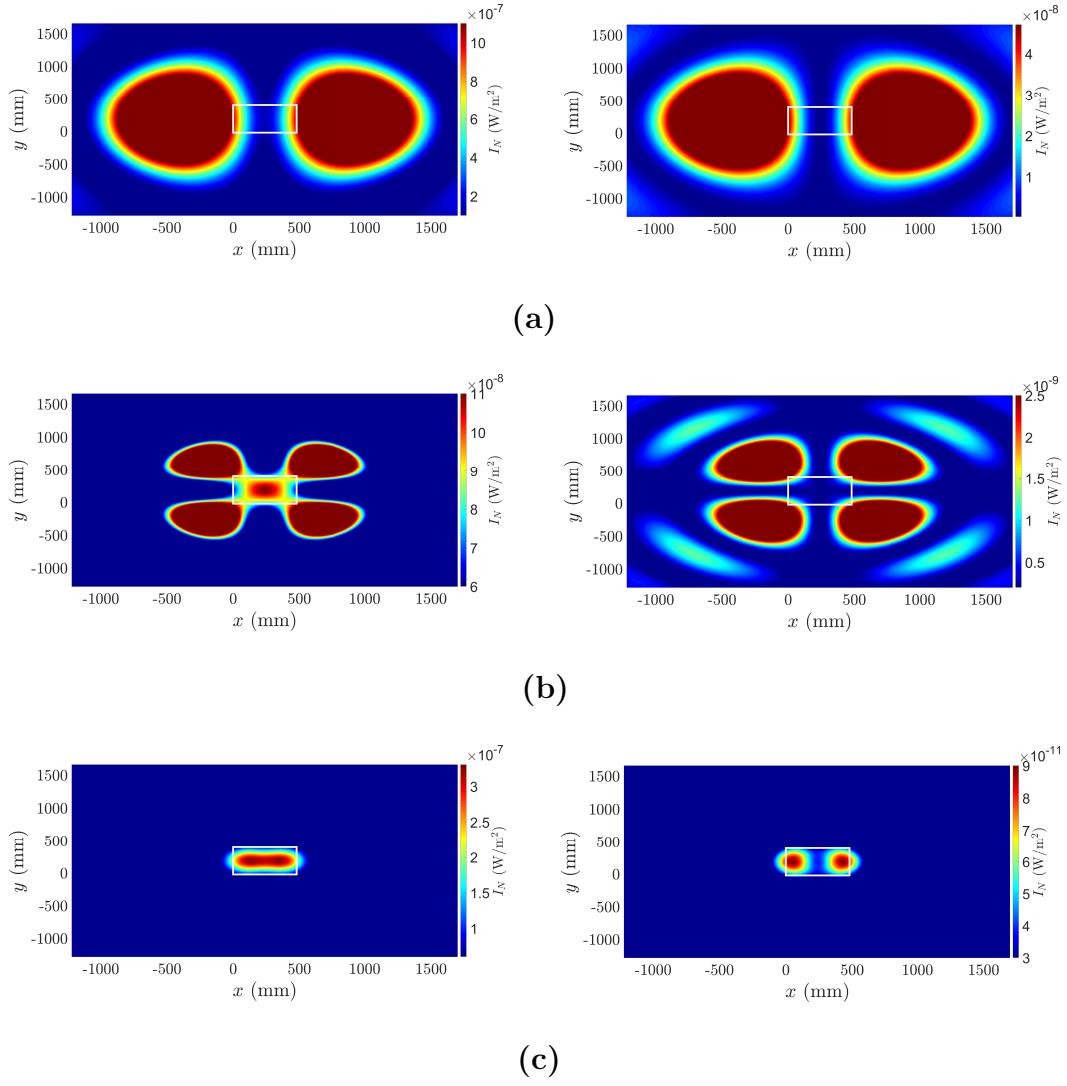


Figure 9: Comparison of the NNI between the panel under ADF excitation (left column) and under TBL excitation (right column) over a large surface at $z = 0$ for selected frequencies of (a) 177 Hz, (b) 307 Hz, (c) 630 Hz.

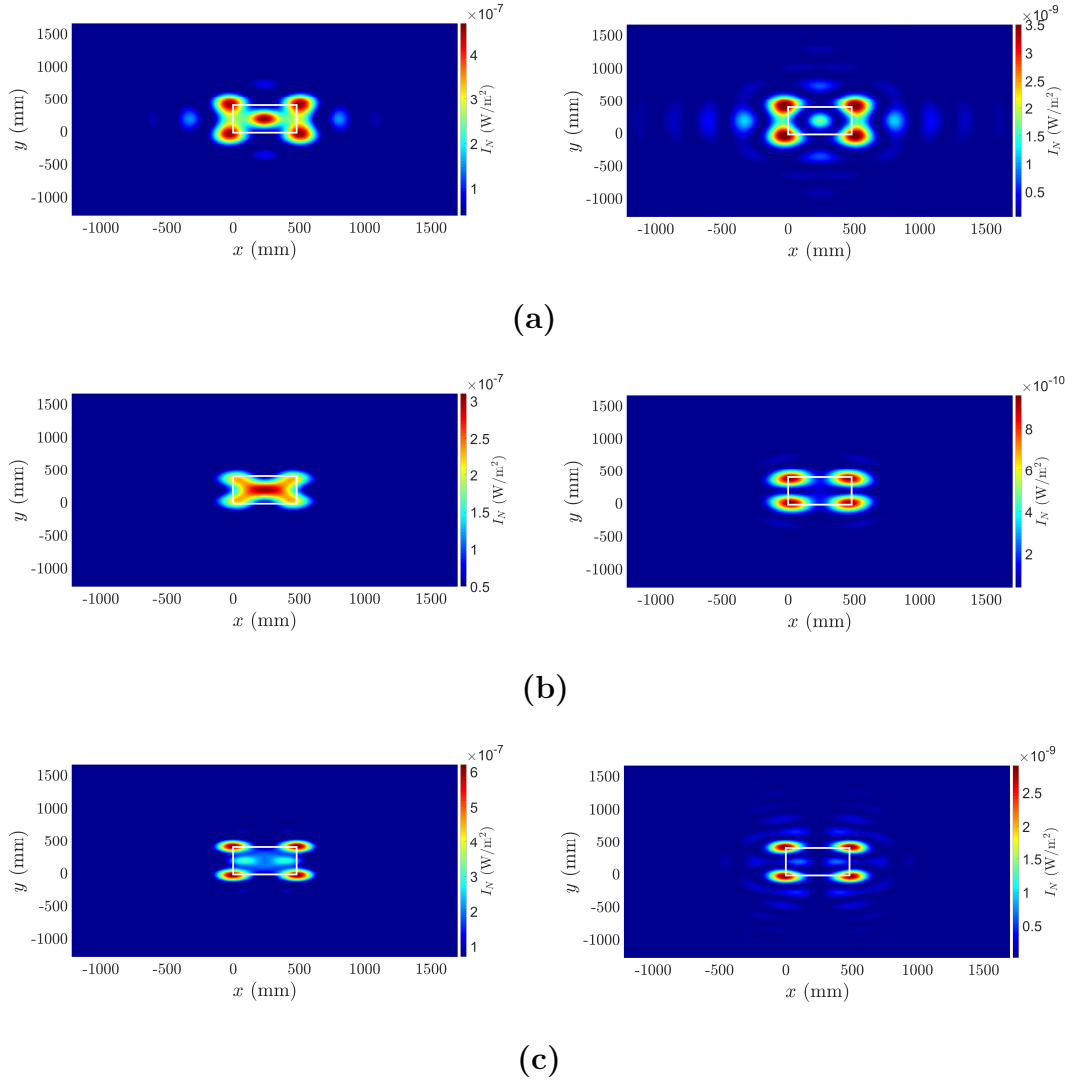


Figure 10: Comparison of the NNI between the panel under ADF excitation (left column) and under TBL excitation (right column) over a large surface at $z = 0$ for selected frequencies of (a) 691 Hz, (b) 700 Hz and (c) 924 Hz.

393 **6. Conclusions**

394 The non-negative intensity was analytically formulated in wavenumber
 395 domain for planar structures subject to random excitations. To calculate
 396 the NNI, the CSD of the stochastic field and either the sensitivity function
 397 of pressure or normal fluid particle velocity were required. The proposed
 398 formulation can be used for both infinite planar structure and finite plate
 399 in an infinite baffle. The NNI was used to quantify the regions on a simply
 400 supported baffled panel excited by the TBL and ADF which radiate energy
 401 to the far field. Comparing maps of the ASD of the pressure and panel
 402 velocity, and active intensity with those of the NNI at different frequencies
 403 revealed that the NNI is a powerful tool to identify hot spots on the panel
 404 surface which contribute to the sound power. It was also found that the NNI
 405 distribution is dependent on the excitation type as well as on the frequency of
 406 excitation. It was shown that the more the NNI distribution is concentrated
 407 within the panel surface, the higher the radiation efficiency becomes. In other
 408 word, high radiation efficiency can be achieved if the most area of the panel
 409 contributes to the radiated sound power, and this can be identified using the
 410 NNI.

411 **Acknowledgments**

412 This research was supported by the Australian Government through the
 413 Australian Research Council’s Discovery Early Career Project funding scheme
 414 (project DE190101412).

415 **Appendix A: The normalized CSD function of TBL and ADF ex-**
 416 **citations**

417 *The Mellen model*

418 The Mellen normalized wavenumber-frequency model is given by [37]

$$\tilde{\phi}_{pp}^{\text{TBL}}(k_x, k_y, \omega) = \frac{2\pi(\alpha_x\alpha_y)^2 k_c}{((\alpha_x\alpha_y k_c)^2 + (\alpha_x k_y)^2 + \alpha_y^2 (k_x - k_c)^2)^{3/2}}, \quad (\text{A.1})$$

419 where $k_c = \omega/U_c$, $\alpha_x = 0.1$ and $\alpha_y = 0.77$.

420 *The ADF model*

421 The normalised CSD function of the ADF in the wavenumber-frequency
422 space is given by [42].

$$\tilde{\phi}_{pp}^{\text{ADF}}(k_x, k_y, \omega) = \left\{ \begin{array}{ll} \frac{2\pi}{k_a \sqrt{k_a^2 - k_x^2 - k_y^2}}, & k_a^2 > k_x^2 + k_y^2 \\ 0, & k_a^2 \leq k_x^2 + k_y^2 \end{array} \right\}, \quad (\text{A.2})$$

423 **References**

- 424 [1] M. B. S. Magalhães, R. A. Tenenbaum, Sound sources reconstruction
425 techniques: A review of their evolution and new trends, *Acta. Acust.*
426 *united. Ac.* 90 (2) (2004) 199–220.
- 427 [2] E. G. Williams, Supersonic acoustic intensity, *J. Acoust. Soc. Am.* 97 (1)
428 (1995) 121–127.
- 429 [3] E. G. Williams, Supersonic acoustic intensity on planar sources, *J.*
430 *Acoust. Soc. Am.* 104 (5) (1998) 2845–2850.
- 431 [4] E. Fernandez-Grande, F. Jacobsen, Q. Leclere, Direct formulation of
432 the supersonic acoustic intensity in space domain, *J. Acoust. Soc. Am.*
433 131 (1) (2012) 186–193.
- 434 [5] E. Fernandez-Grande, F. Jacobsen, Conservation of power of the super-
435 sonic acoustic intensity, *J. Acoust. Soc. Am.* 136 (2) (2014) 461–465.
- 436 [6] N. P. Valdivia, E. G. Williams, P. C. Herdic, Equivalent sources method
437 for supersonic intensity of arbitrarily shaped geometries, *J. Sound. Vib.*
438 347 (2015) 46–62.
- 439 [7] M. B. S. Magalhães, R. A. Tenenbaum, Supersonic acoustic intensity
440 for arbitrarily shaped sources, *Acta. Acust. united. Ac.* 92 (2) (2006)
441 189–201.
- 442 [8] S. Marburg, E. Lösche, H. Peters, N. Kessissoglou, Surface contributions
443 to radiated sound power, *J. Acoust. Soc. Am.* 133 (6) (2013) 3700–3705.
- 444 [9] E. G. Williams, Convolution formulations for non-negative intensity, *J.*
445 *Acoust. Soc. Am.* 134 (2) (2013) 1055–1066.

- 446 [10] C. C. Junior, R. Tenenbaum, Useful intensity: A technique to identify
447 radiating regions on arbitrarily shaped surfaces, *J. Sound. Vib.* 332 (6)
448 (2013) 1567–1584.
- 449 [11] V. Ferreira, R. Tenenbaum, F. Dias, C. Corrêa Jr, Power operator di-
450 mensional reduction to obtain the useful intensity in rectangular plates
451 with several boundary conditions, *J. Sound. Vib.* 448 (2019) 130–145.
- 452 [12] D. Liu, H. Peters, S. Marburg, N. Kessissoglou, Surface contributions
453 to scattered sound power using non-negative intensity, *J. Acoust. Soc.*
454 *Am.* 140 (2) (2016) 1206–1217.
- 455 [13] D. Liu, H. Peters, S. Marburg, N. Kessissoglou, Supersonic intensity and
456 non-negative intensity for prediction of radiated sound, *J. Acoust. Soc.*
457 *Am.* 139 (5) (2016) 2797–2806.
- 458 [14] D. Liu, Z. Havránek, S. Marburg, H. Peters, N. Kessissoglou, Non-
459 negative intensity and back-calculated non-negative intensity for anal-
460 ysis of directional structure-borne sound, *J. Acoust. Soc. Am.* 142 (1)
461 (2017) 117–123.
- 462 [15] D. Liu, S. Marburg, C. Geweth, N. Kessissoglou, Non-negative intensity
463 for structures with inhomogeneous damping, *J. Theor. Comput. Acoust.*
464 27 (01) (2019) 1850050.
- 465 [16] D. R. Wilkes, H. Peters, P. Croaker, S. Marburg, A. J. Duncan,
466 N. Kessissoglou, Non-negative intensity for coupled fluid–structure in-
467 teraction problems using the fast multipole method, *J. Acoust. Soc. Am.*
468 141 (6) (2017) 4278–4288.
- 469 [17] M. Aucejo, N. Totaro, J.-L. Guyader, Identification of source veloci-
470 ties on 3D structures in non-anechoic environments: Theoretical back-
471 ground and experimental validation of the inverse patch transfer func-
472 tions method, *J. Sound. Vib.* 329 (18) (2010) 3691–3708.
- 473 [18] D. Vigoureux, N. Totaro, J. Lagneau, J.-L. Guyader, Inverse patch
474 transfer functions method as a tool for source field identification, *J.*
475 *Vib. Acoust.* 137 (2).
- 476 [19] N. P. Valdivia, Integral formulas for supersonic reconstruction of the
477 acoustic field, *Inverse. Probl. Eng.* 26 (3) (2018) 376–397.

- 478 [20] N. P. Valdivia, Improved integral formulae for supersonic reconstruction
479 of the acoustic field, *Inverse. Probl. Eng.* 26 (6) (2018) 898–924.
- 480 [21] E. Ciappi, S. De Rosa, F. Franco, J. Guyader, S. Hambric, *Flinovia*
481 - Flow Induced Noise and Vibration Issues and Aspects: A Focus on
482 Measurement, Modeling, Simulation and Reproduction of the Flow Ex-
483 citation and Flow Induced Response, EBL-Schweitzer, Springer Inter-
484 national Publishing Switzerland, 2014.
- 485 [22] E. Ciappi, S. De Rosa, F. Franco, J. Guyader, S. Hambric, R. Le-
486 ung, A. Hanford, *Flinovia-Flow Induced Noise and Vibration Issues and*
487 *Aspects-II: A Focus on Measurement, Modeling, Simulation and Repro-*
488 *duction of the Flow Excitation and Flow Induced Response*, Springer
489 International Publishing Switzerland, 2018.
- 490 [23] M. Karimi, P. Croaker, A. Skvortsov, D. Moreau, N. Kessissoglou, Nu-
491 merical prediction of turbulent boundary layer noise from a sharp-edged
492 flat plate, *Int. J. Numer. Meth. Fl.* 90 (2019) 522–543.
- 493 [24] E. G. Williams, *Fourier acoustics: sound radiation and nearfield acous-*
494 *tical holography*, Elsevier, San Diego, California, USA, 1999.
- 495 [25] C. Marchetto, Experimental characterization of the vibroacoustic
496 response of panels under random excitations by sensitivity func-
497 tions, Ph.D. thesis, Univ Lyon, INSA-Lyon, Laboratoire Vibrations-
498 Acoustique (LVA), France (2018).
- 499 [26] M. Karimi, L. Maxit, P. Croaker, O. Robin, A. Skvortsov, S. Marburg,
500 N. Atalla, N. Kessissoglou, Analytical and numerical prediction of acous-
501 tic radiation from a panel under turbulent boundary layer excitation, *J.*
502 *Sound. Vib.* (2020) 115372.
- 503 [27] A. Ghatak, S. Lokanathan, *The Dirac Delta Function*, Springer Nether-
504 lands, Dordrecht, 2004, pp. 3–18.
- 505 [28] X.-W. Gao, An effective method for numerical evaluation of general 2D
506 and 3D high order singular boundary integrals, *Comput. Methods in*
507 *Appl. Mech. Eng.* 199 (45-48) (2010) 2856–2864.
- 508 [29] K. M. Singh, M. Tanaka, Analytical integration of weakly singular inte-
509 grals in boundary element analysis of Helmholtz and advection-diffusion

- 510 equations, *Comput. Methods in Appl. Mech. Eng.* 189 (2) (2000) 625–
511 640.
- 512 [30] C. Maury, P. Gardonio, S. Elliott, A wavenumber approach to modelling
513 the response of a randomly excited panel, Part I: General theory, *J.*
514 *Sound. Vib.* 252 (1) (2002) 83–113.
- 515 [31] D. E. Newland, *An introduction to random vibrations, spectral &*
516 *wavelet analysis*, Courier Corporation, Mineola, New York, USA, 2012.
- 517 [32] M. Karimi, P. Croaker, L. Maxit, O. Robin, A. Skvortsov, S. Marburg,
518 N. Kessissoglou, A hybrid numerical approach to predict the vibrational
519 responses of panels excited by a turbulent boundary layer, *J. Fluid.*
520 *Struct.* 92 (2020) 102814.
- 521 [33] L. Maxit, O. Guasch, V. Meyer, M. Karimi, Noise radiated from a peri-
522 odically stiffened cylindrical shell excited by a turbulent boundary layer,
523 *J. Sound. Vib.* 466 (2020) 115016.
- 524 [34] L. Maxit, M. Karimi, V. Meyer, N. Kessissoglou, Vibroacoustic re-
525 sponses of a heavy fluid loaded cylindrical shell excited by a turbulent
526 boundary layer, *J. Fluid. Struct.* 92 (2020) 102758.
- 527 [35] L. Maxit, Simulation of the pressure field beneath a turbulent boundary
528 layer using realizations of uncorrelated wall plane waves, *J. Acoust. Soc.*
529 *Am.* 140 (2) (2016) 1268–1285.
- 530 [36] W. Graham, A comparison of models for the wavenumber–frequency
531 spectrum of turbulent boundary layer pressures, *J. Sound. Vib.* 206 (4)
532 (1997) 541–565.
- 533 [37] R. Mellen, Wave-vector filter analysis of turbulent flow, *J. Acoust. Soc.*
534 *Am.* 95 (3) (1994) 1671–1673.
- 535 [38] M. Bull, Wall-pressure fluctuations associated with subsonic turbulent
536 boundary layer flow, *J. Fluid. Mech.* 28 (4) (1967) 719–754.
- 537 [39] C. Marchetto, L. Maxit, O. Robin, A. Berry, Experimental prediction
538 of the vibration response of panels under a turbulent boundary layer
539 excitation from sensitivity functions, *J. Acoust. Soc. Am.* 143 (5) (2018)
540 2954–2964.

- 541 [40] Z. Dingguo, M. J. Crocker, Sound power radiated from rectangular
542 plates, *Arch. Acoust.* 34 (1) (2009) 25–39.
- 543 [41] G. Maidanik, Response of ribbed panels to reverberant acoustic fields,
544 *J. Acoust. Soc. Am.* 34 (6) (1962) 809–826.
- 545 [42] C. Marchetto, L. Maxit, O. Robin, A. Berry, Vibroacoustic response of
546 panels under diffuse acoustic field excitation from sensitivity functions
547 and reciprocity principles, *J. Acoust. Soc. Am.* 141 (6) (2017) 4508–4521.